CHAPTER III
RESUTS AND DISCUSSION

3.1 Tolerance factor

The stability of perovskite structure of all prepared compounds was determined by tolerance factors (*t*). These factors were calculated based on chemical formulae using ionic crystal radii as tabulated by Shannon and Prewitt (Appendix A). The calculated *t* values of all prepared oxides are listed in Table 3.1.

Table 3.1 The tolerance factors of all prepared oxides

a) $(La_{0.8}Sr_{0.2})_{2-x}Ca_xNiO_4$ (LSN-Ca_x)

Compounds	*t*
LSN	0.891
LSN-$Ca_{0.1}$	0.891
LSN-$Ca_{0.2}$	0.890
LSN-$Ca_{0.3}$	0.889
LSN-$Ca_{0.4}$	0.888
LSN-$Ca_{0.5}$	0.887

b) $(La_{0.8}Sr_{0.2})_{2-x}Ca_xNi_{0.9}Co_{0.1}O_4$ (LSNC-Ca_x)

Compounds	*t*
LSNC	0.889
LSNC-$Ca_{0.1}$	0.888
LSNC-$Ca_{0.2}$	0.887
LSNC-$Ca_{0.3}$	0.886
LSNC-$Ca_{0.4}$	0.885
LSNC-$Ca_{0.5}$	0.884

c) $La_2Ni_{0.89-y}Co_{0.1}M_yO_4$ (LNC-Fe_y or LNC-Zn_y)

Compounds	*t*
LNC	0.883
LNC-$Fe_{0.01}$	0.882
LNC-$Fe_{0.03}$	0.882
LNC-$Fe_{0.05}$	0.881
LNC-$Fe_{0.1}$	0.879
LNC-$Fe_{0.2}$	0.875

Compounds	*t*
LNC	0.883
LNC-$Zn_{0.01}$	0.883
LNC-$Zn_{0.03}$	0.882
LNC-$Zn_{0.05}$	0.882
LNC-$Zn_{0.1}$	0.881
LNC-$Zn_{0.2}$	0.879

d) $La_{2-x}Ca_xNi_{0.85}Co_{0.1}M_{0.05}O_4$ (LNCF-Ca_x or LNCZ-Ca_x)

Compounds	*t*
LNCF	0.881
LNCF -$Ca_{0.1}$	0.880
LNCF -$Ca_{0.3}$	0.879
LNCF -$Ca_{0.5}$	0.878
LNCF -$Ca_{0.7}$	0.877

Compounds	*t*
LNCZ	0.882
LNCZ -$Ca_{0.1}$	0.881
LNCZ -$Ca_{0.3}$	0.880
LNCZ -$Ca_{0.5}$	0.879
LNCZ -$Ca_{0.7}$	0.878

The perovskite structure is stable when *t* value locate in the range of $0.75<t<1.0$ [33]. As *t* tends to 1, the structure is closer to the ideal cubic structure. The cubic structure can be maintained with $0.95<t<1.04$, while $0.75<t<0.9$ low-symmetry orthorhombic or tetragonal structure will be obtained [19, 39]. It can be seen from Table 3.1 that the *t* values of all prepared oxides vary from 0.877 to 0.891 and they are larger than 0.75 indicating the ability to form stable perovskite structure. However, the tolerance factors are less than 0.95. This means that they do not have a cubic structure. When A-site cation is substituted by Ca^{2+}, whose ionic radius is smaller than that of A-site cation (La^{3+} and Sr^{2+}) or substitution of B-site cation (Ni^{2+}) by larger cation (Fe^{2+} and Zn^{2+}), the *t* value decreases. This indicates that the unit cell is distorted resulting in the change of lattice structure from cubic to another structure such as tetragonal structure.

3.2 Synthesis and properties of $(La_{0.8}Sr_{0.2})_{2-x}Ca_xNiO_4$ (LSN-Ca_x)

LSN-Ca_x (x=0, 0.1, 0.2, 0.3, 0.4 and 0.5) were synthesized and sintered at 1350°C for 10 hours. The obtained samples were characterized for phase structure, surface morphology and conducting property by XRD, SEM and DC 4-probe method, respectively. LSN-Ca_x with the highest electrical conductivity was chosen for testing the single cell performance.

3.2.1 XRD analyses

Figure 3.1 shows the XRD patterns of LSN-Ca_x sintered at 1350°C for 10 hours. All the diffraction peaks can be indexed as K_2NiF_4-type with tetragonal structure (JCPDS 89-8309). It is noticed that the main diffraction peaks of LSN-Ca_x shift to higher values of 2θ compared to the undoped one. This shift is resulted from the shrinkage of crystal lattice caused by substitution of La^{3+} (r=1.36 Å) and Sr^{2+} (r=1.45 Å) with Ca^{2+} (r=1.32 Å), as explained by Bragg's law in equation 3.1.

$$2d \sin\theta = n\lambda \qquad (3.1)$$

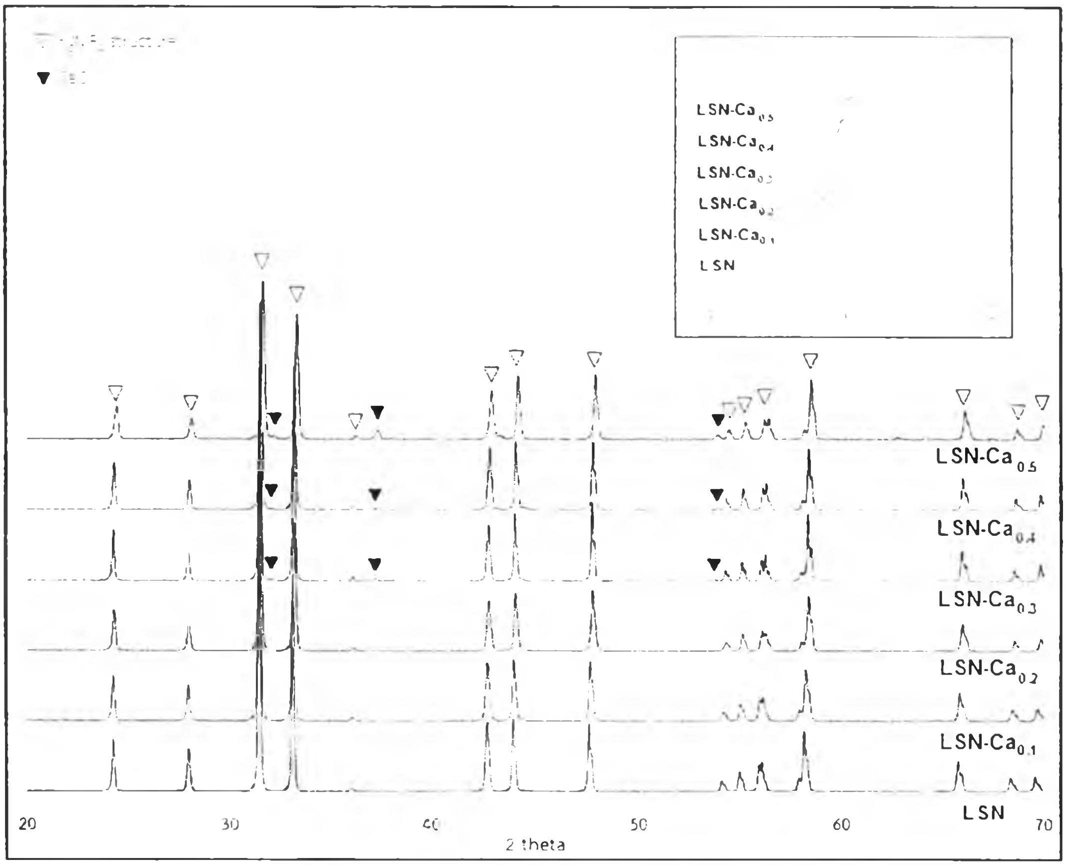

Figure 3.1 XRD patterns of LSN-Ca_x (x=0-0.5) discs sintered at 1350°C for 10 hours

The lattice parameters *a*, *c* and the unit cell volume decrease with the calcium content as presented in Table 3.2. This shrinkage of lattice parameters can be attributed to two factors. Firstly, the substitution of low valence cations (Ca^{2+}) will induce the oxidation state of B-site cations in the ABO_3 layer from Ni^{2+}, Ni^{3+} to Ni^{4+} due to the electroneutrality condition. From the valence bond theory, in this case the Ni-O bond strength will increase and the bond length decreases [40]. Secondly, the substitution of smaller cations on the A-site will affect the A-O bond in the rock salt layer resulting in the shrinkage of A-O bond [41].

Table 3.2 Lattice parameter and unit cell volume of LSN-Ca$_x$ (x=0-0.5)

Compound	* Lattice parameter		V (Å^3)
	a (Å)	*c* (Å)	
LSN	3.819	12.741	185.77
LSN-Ca$_{0.1}$	3.818	12.719	185.37
LSN-Ca$_{0.2}$	3.813	12.687	184.46
LSN-Ca$_{0.3}$	3.816	12.690	184.80
LSN-Ca$_{0.4}$	3.811	12.684	184.22
LSN-Ca$_{0.5}$	3.820	12.665	184.78

*The average lattice parameters are calculated from the diffraction peaks of (101), (103), (110), (114) and (200) planes.

In addition, the formation of CaO (JCPDS 48-1467) is observed for x>0.2. At x=0-0.2, there are no secondary phase appeared. Therefore, the limitation of Ca^{2+} addition in LSN is considered to be less than 0.3.

3.2.2 SEM analyses

LSN, LSN-Ca$_{0.1}$ and LSN-Ca$_{0.2}$ discs without impurity phase were chosen to study the surface morphology. The reduction of porosity and the agglomeration of grains were determined by SEM images in Figure 3.2. When LSN is substituted by Ca^{2+} in the A-site, the dense microstructure with few isolated pores and large grain sizes are obtained.

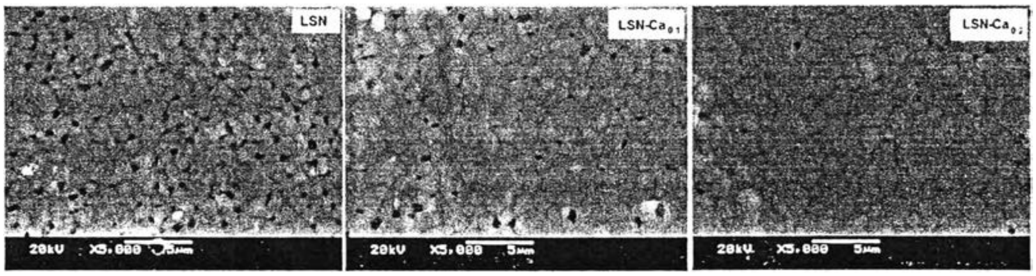

Figure 3.2 SEM images of LSN-Ca$_x$ (x=0, 0.1 and 0.2) discs

The increase in Ca^{2+} substitution promotes the higher grain size and the large density of materials which is consistent with the result of relative density calculation as shown in Table 3.3.

Table 3.3 Average grain size and relative density of LSN-Ca$_x$ (x=0, 0.1 and 0.2) discs

Sample	Grain size (μm)	Relative density (%)
LSN	0.94	80.60
LSN-Ca$_{0.1}$	1.42	82.27
LSN-Ca$_{0.2}$	1.88	95.18

3.2.3 Electrical conductivity analyses

Figure 3.3 shows the Ca-doping level and electrical conductivity of LSN-Ca$_x$ as a function of temperature. Moreover, the data are summarized in Table 3.4.

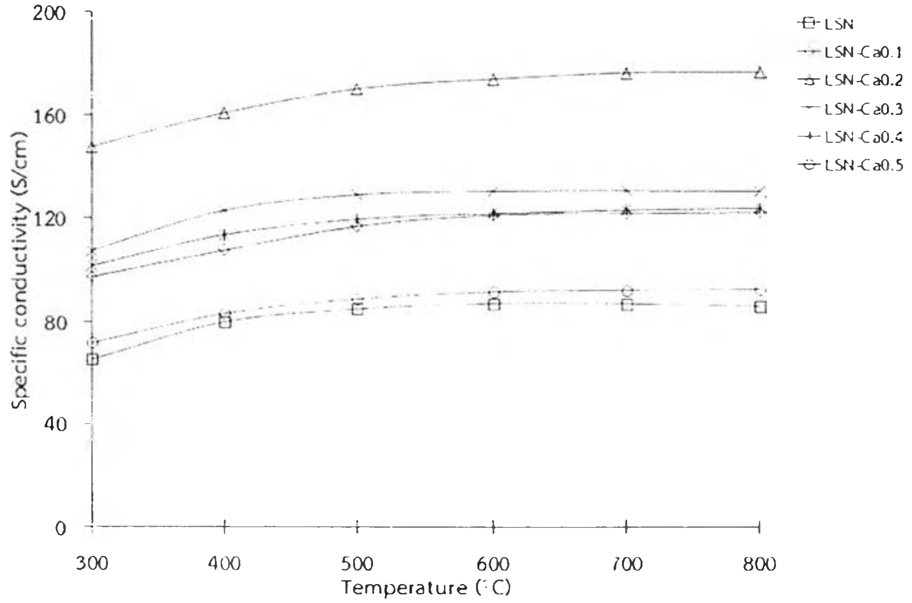

Figure 3.3 Temperature dependence of the specific conductivity (σ) of LSN-Ca$_x$ (x=0-0.5)

The electrical conductivity of all samples shows an identical variation with temperature. It increases with increasing temperature and then remains constant at elevating temperature because at high temperature, phonon concentration increases and causes lattice scattering which lowers the electron mobility. Moreover the loss of lattice oxygen at high temperature results in the generation of oxygen vacancies [42] and the reduction of the number of conductivity carriers as expressed in equation 3.2.

$$O_o^x \rightarrow \frac{1}{2}O_{2(g)} + V_o^{\bullet\bullet} + 2e^- \qquad (3.2)$$

where O_o^x = an oxide ion on an oxide ion lattice site, with neutral charge
$V_o^{\bullet\bullet}$ = oxygen vacancies

At each temperature, the electrical conductivity increases with calcium content and reaches a maximum value at x=0.2, followed by a decrease of electrical conductivity with more Ca-doping (x=0.3, 0.4 and 0.5), but it is still higher than the undoped one. The conductivity increases with calcium due to the increasing concentration of electron holes in material as charge compensation of Ca-doping on A-site as described in equation 3.3

$$Ca'_{La} \rightarrow Ni_{Ni}^{\bullet} + V_o^{\bullet\bullet} \qquad (3.3)$$

where Ca'_{La} = a calcium ion on a lanthanum ion lattice site, with singular negative charge
$Ni_{Ni}^{\bullet}$ = a nickel ion on a nickel ion lattice site, with singular positive charge
$V_o^{\bullet\bullet}$ = oxygen vacancies

Based on defect chemistry theory, the electron holes can be obtained by the change in valence state of B-site ions. In this case, the partial replacement of A-site cation with lower valent cation (Ca^{2+}) leads to the change of B-site cation from Ni^{3+} to Ni^{4+} that would introduce electronic conductivity (electron holes by $Ni_{Ni^{3+}}^{4+\bullet}$). Moreover, the increasing of conductivity can be explained by the increased overlapping of the atomic orbits. From previous XRD results, lattice parameters *a* and *c* decreased with increasing Ca^{2+} substitution. This was indicated that the bond length of Ni-O-Ni reduced and the overlapping of the atomic orbitals between the adjacent Ni was promoted leading to the fast migration of electron. Therefore the conductivity increases.

The decreased electrical conductivity of samples with x=0.3, 0.4 and 0.5 is mainly due to the appearance of impurity (CaO) as recognized by XRD. Moreover it may associate with the distorted unit cells with increasing calcium content causing the small orbital overlap. This will be unfavorable to the charge carrier transfer in materials [43].

Table 3.4 The specific conductivity of LSN-Ca$_x$ (x = 0-0.5)

Sample	Specific conductivity (S/cm)						
	300°C	400°C	500°C	600°C	700°C	800°C	σ_{max} (T, °C)
LSN	65.2	80.0	85.1	87.3	87.2	86.4	87.3 (600)
LSN-Ca$_{0.1}$	97.4	107.8	117.1	121.3	122.0	122.4	122.4 (800)
LSN-Ca$_{0.2}$	147.7	160.8	170.3	174.2	176.7	176.9	176.9 (800)
LSN-Ca$_{0.3}$	107.6	123.1	129.2	130.7	130.9	130.6	130.9 (700)
LSN-Ca$_{0.4}$	101.6	113.7	119.8	122.1	123.3	124.1	124.1 (800)
LSN-Ca$_{0.5}$	71.8	83.3	89.0	91.8	92.5	92.9	92.9 (800)

In addition, the relative density has a dramatic effect on the electrical conductivity of materials. The dense microstructure can contribute to an increase of the bulk conductivity. The sample with x=0.2 which density is higher than others offers a maximum electrical conductivity of 176.9 S/cm at 800°C.

The Arrhenius plot for electrical conductivity of samples is shown in Figure 3.4. The linear relationship between ln(σT) and 1000/T demonstrates a semiconducting behavior, which the electrical conduction occurs by thermally activated hopping of small polarons [44]. With increasing temperature, the hoping of small polarons increases. The slope of the linear part of Arrhenius plot can determine the activation energy (E_a) values in Table 3.5.

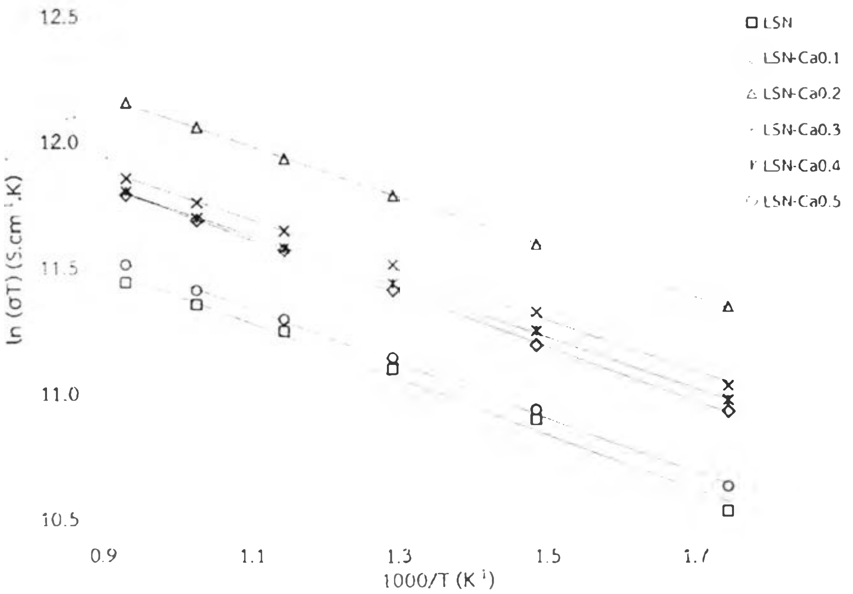

Figure 3.4 Arrhenius plot of the electrical conductivity of LSN-Ca$_x$ (x=0-0.5)

Table 3.5 Activation energy (E_a) of LSN-Ca_x (x=0-0.5) at 300-800°C

Sample	E_a (kJ/mol)
LSN	9.2
LSN-$Ca_{0.1}$	8.8
LSN-$Ca_{0.2}$	8.3
LSN-$Ca_{0.3}$	8.3
LSN-$Ca_{0.4}$	8.4
LSN-$Ca_{0.5}$	9.0

The E_a value is used to determine the electron hopping. The lower the value of E_a, the faster the hopping of electrons. The lowest E_a value was obtained for x=0.2 which corresponds to the highest conductivity of LSN-$Ca_{0.2}$ in this work.

3.3 Synthesis and properties of $(La_{0.8}Sr_{0.2})_{2-x}Ca_xNi_{0.9}Co_{0.1}O_4$ (LSNC-Ca_x)

LSNC-Ca_x (x=0, 0.1, 0.2, 0.3, 0.4 and 0.5) were synthesized and sintered at 1350°C for 10 hours. The obtained samples were characterized for phase structure, surface morphology and conducting property by XRD, SEM and DC 4-probe method, respectively. LSNC-Ca_x with the highest electrical conductivity was chosen for testing the single cell performance.

3.3.1 XRD analyses

The XRD patterns of LSNC-Ca_x (Figure 3.5) show the similar result with LSN-Ca_x. These patterns reveal the K_2NiF_4-type with tetragonal structure. It is observed that the peaks are slightly shifted to higher angle with increasing the calcium content. It confirms that Ca occupies a part of La and Sr sites in crystal lattice. When A-site cations are substituted by low valence cations, the average oxidation state of B-site cations will increase, causing the change in crystal structure. In this case, Ni^{2+} and Co^{2+} are oxidized to small size cations therefore the lattice parameter is diminished. The lattice parameters *a*, *c* and the unit cell volume of LSNC-Ca_x were calculated in Table 3.6.

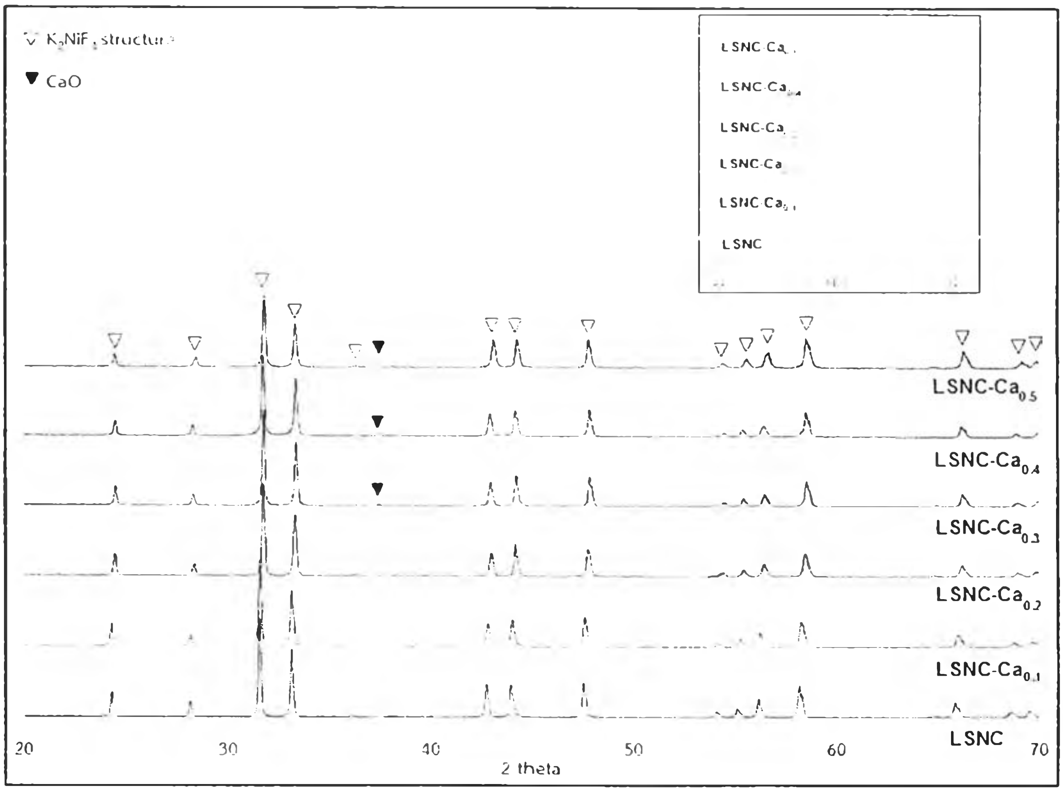

Figure 3.5 XRD patterns of LSNC-Ca_x (x=0-0.5) discs sintered at 1350°C for 10 hours

Table 3.6 Lattice parameter and unit cell volume of LSNC-Ca_x (x=0-0.5)

Compound	* Lattice parameter		V (Å^3)
	a (Å)	*c* (Å)	
LSNC	3.819	12.741	185.77
LSNC-$Ca_{0.1}$	3.818	12.719	185.37
LSNC-$Ca_{0.2}$	3.813	12.687	184.46
LSNC-$Ca_{0.3}$	3.816	12.690	184.80
LSNC-$Ca_{0.4}$	3.820	12.665	184.78
LSNC-$Ca_{0.5}$	3.811	12.684	184.22

*The average lattice parameter is calculated from the diffraction peaks of (101), (103), (110), (114) and (200) planes.

The formation of CaO impurity phase is observed in composition of x>0.2, which is recognized from the main peak at 2θ of 37.5°. Therefore, it is considered that the limitation of Ca addition in LSNC is less than 0.3.

3.3.2 SEM analyses

LSNC, LSNC-Ca$_{0.1}$ and LSNC-Ca$_{0.2}$ discs with pure single phase structure were chosen to study the surface morphology. From SEM images in Figure 3.6, LSNC exhibits porous surface materials. With increasing the calcium substitution, the grain size increases and no porosity are observed in sample with x= 0.2. The average grain size and the calculated relative density were listed in Table 3.7. It is found that the relative density increases from approximately 84% for LSNC to 91% for LSNC-Ca$_{0.2}$, suggesting that substitution of calcium enhances the density of LSNC-Ca$_x$ in this work.

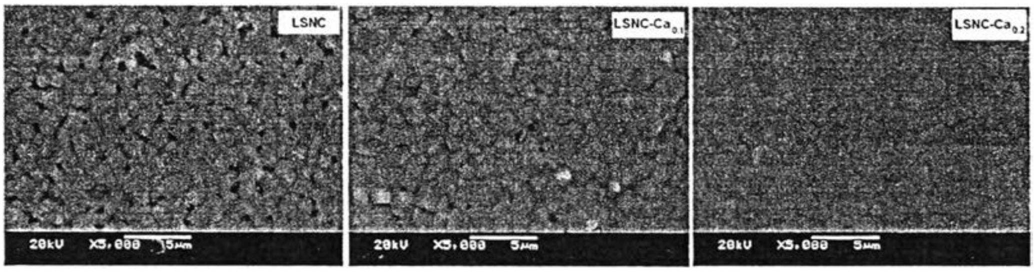

Figure 3.6 SEM images of LSNC-Ca$_x$ (x=0, 0.1 and 0.2) discs

Table 3.7 Average grain size and relative density of LSNC-Ca$_x$ (x=0, 0.1 and 0.2) discs

Sample	Grain size (μm)	Relative density (%)
LSNC	1.02	84.07
LSNC-Ca$_{0.1}$	1.39	90.69
LSNC-Ca$_{0.2}$	2.06	91.47

3.3.3 Electrical conductivity analyses

Figure 3.7 represents the temperature dependence of electrical conductivity as a function of Ca-doping concentrations and the data are summarized in Table 3.8.

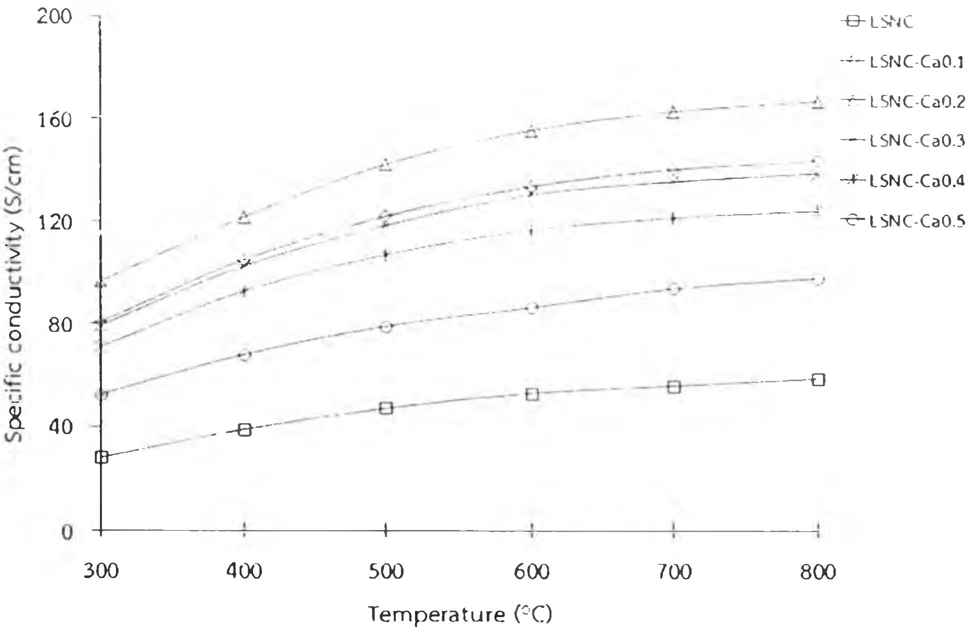

Figure 3.7 Temperature dependence of the specific conductivity (σ) of LSNC-Ca_x (x=0-0.5)

It is observed that the electrical conductivity of all LSNC-Ca_x samples exhibits semiconducting behavior. It increases with increasing temperature. Moreover the calcium substitution on A-site in LSNC affects the electrical conductivity. The conductivity increases with the calcium content and reaches a maximum value for sample with x=0.2. This result can be explained by the increasing of concentration and mobility of electron holes. The replacement of La^{3+} with Ca^{2+} results in the production of electron holes in Ni site and Co site or the formation of oxygen vacancies [45]. The individual defect equilibrium can be described by equation 3.4.

$$[Ca'_{La}] \rightarrow [Ni^{\bullet}_{Ni}] + [Co^{\bullet}_{Co}] + 2[V^{\bullet\bullet}_{O}] \tag{3.4}$$

where Ca'_{La} = a calcium ion on a lanthanum ion lattice site, with singular negative charge

$Ni^{\bullet}_{Ni}$ = a nickel ion on a nickel ion lattice site, with singular positive charge

$Co^{\bullet}_{Co}$ = a cobalt ion on a cobalt ion lattice site, with singular positive charge

$V^{\bullet\bullet}_{O}$ = oxygen vacancies

The highest electrical conductivity is achieved for LSNC-$Ca_{0.2}$ and the value is 166.9 S/cm at 800°C. The conductivity decreases with the composition of x>0.2. This may be due to the appearance of impurity phase (CaO) which has low electrical conductivity.

Table 3.8 The specific conductivity of LSNC-Ca_x (x=0-0.5)

Sample	Specific conductivity (S/cm)						
	300°C	400°C	500°C	600°C	700°C	800°C	σ_{max} (T, °C)
LSNC	28.0	38.8	47.2	53.1	56.1	59.0	59.0 (800)
LSNC-$Ca_{0.1}$	80.7	105.1	122.0	133.7	140.4	143.8	143.8 (800)
LSNC-$Ca_{0.2}$	96.6	121.6	142.1	155.5	162.9	166.9	166.9 (800)
LSNC-$Ca_{0.3}$	79.3	102.6	118.4	130.4	135.7	139.0	139.0 (800)
LSNC-$Ca_{0.4}$	70.9	92.8	107.1	116.8	121.6	124.4	124.4 (800)
LSNC-$Ca_{0.5}$	52.4	68.1	79.2	86.6	94.2	98.3	98.3 (800)

The activation energy of LSNC-Ca_x calculated from the slope of Arrhenius plot (Figure 3.8) at 300-800°C is summarized in Table 3.9. The linear relationship between ln(σT) and 1000/T indicates the small polaron conducting mechanism [46]. It can be seen that the E_a value decreases with increasing the calcium content until x=0.2. This can be explained by substitution of calcium leading to the reduction of Ni-O bond length which may result in an easy jump of electron holes [45]. Therefore activation energy for the hopping of electron holes is decreased. When x>0.2, the E_a value increases but it is still lower than the undoped one. The lowest E_a value was obtained for x=0.2 which corresponds to the highest conductivity of LSN-Ca_x in this work.

Table 3. 9 Activation energy (E_a) of LSNC-Ca_x (x=0-0.5) at 300-800°C

Sample	E_a (kJ/mol)
LSNC	14.0
LSNC-$Ca_{0.1}$	12.2
LSNC-$Ca_{0.2}$	12.1
LSNC-$Ca_{0.3}$	12.2
LSNC-$Ca_{0.4}$	12.1
LSNC-$Ca_{0.5}$	12.8

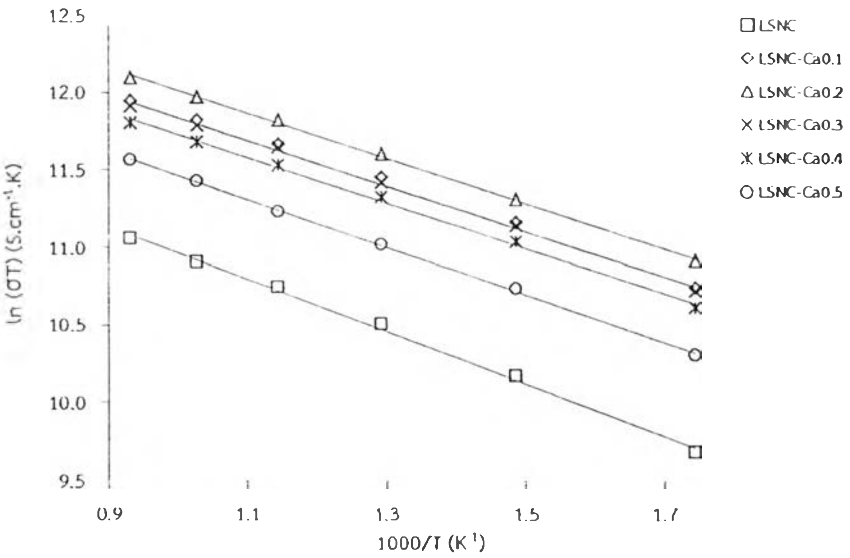

Figure 3.8 Arrhenius plot of the electrical conductivity of LSNC-Ca$_x$ (x=0-0.5)

3.4 Synthesis and properties of $La_2Ni_{0.9-y}Co_{0.1}M_yO_4$ (M=Fe, Zn and y=0-0.2)

LNC-Fe$_y$ and LNC-Zn$_y$ (y=0, 0.01, 003, 0.05, 0.1 and 0.2) were synthesized and sintered at 1350 °C for 10 hours. The obtained samples were characterized for phase structure, surface morphology and oxygen permeation. LNC-Fe$_y$ and LNC-Zn$_y$ with the highest oxygen permeation rate was chosen for substitution of Ca in La-site to improve electrical conductivity in the next experiment.

3.4.1 XRD analyses

The XRD patterns of LNC-Fe$_y$ and LNC-Zn$_y$ are illustrated in Figure 3.9 and 3.10, respectively. The phase is identified as K_2NiF_4-type with tetragonal structure (JCPDS 34-0314). The main diffraction peak around 2θ of 31.5 degree shifts to lower angle with the introduction of iron or zinc, corresponding to an increase in the lattice parameters as presented in Table 3.10 and 3.11. This is due to the fact that the substitution with larger cation (Fe^{2+}=0.92 Å, Zn^{2+}=0.88 Å) causes an expansion in lattice parameters. However, the secondary phase, La_2O_3 (JCPDS 05-0602), is found in the composition of y≥0.1, indicating the limitation of Fe and Zn introduced into the structure. Therefore, LNC-Fe$_y$ and LNC-Zn$_y$ which y<0.1 were selected for further study.

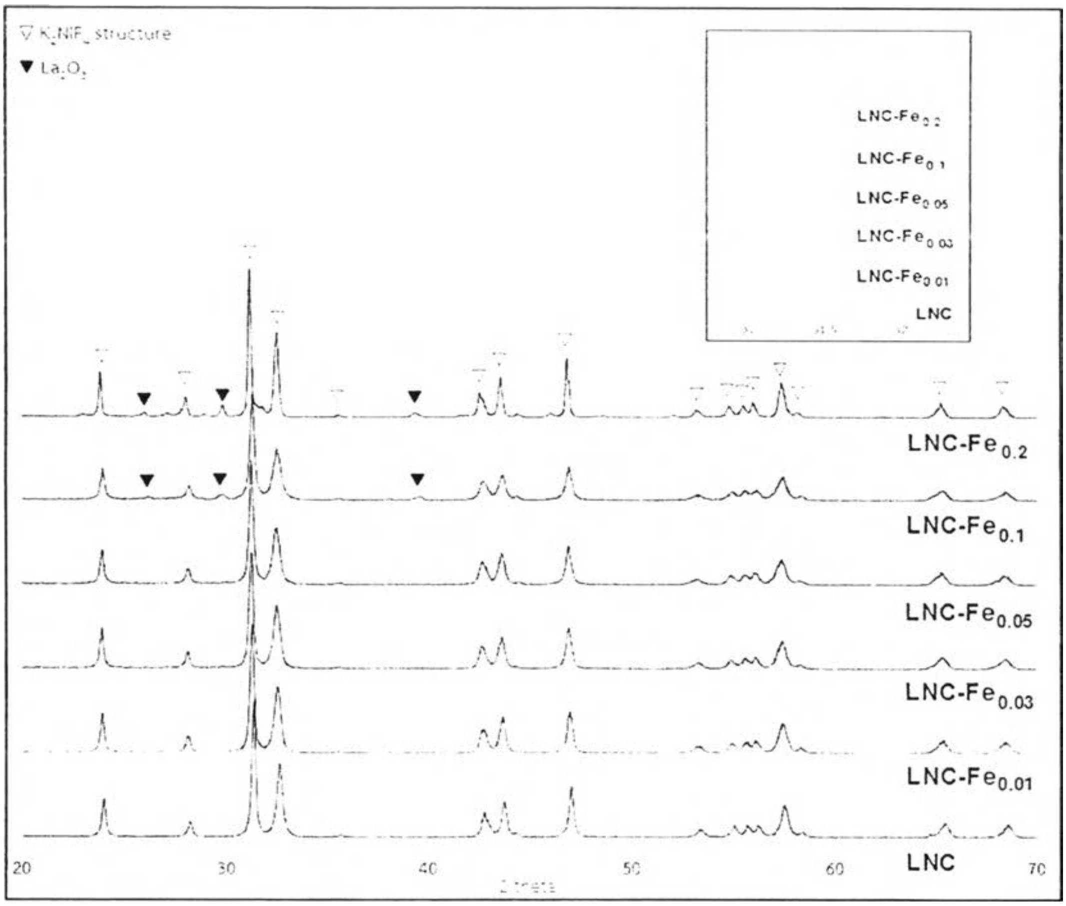

Figure 3.9 XRD patterns of LNC-Fe$_y$ discs sintered at 1350°C for 10 hours

Table 3.10 Lattice parameters and unit cell volume of LNC-Fe$_y$

Compound	* Lattice parameter		V (Å^3)
	a (Å)	*c* (Å)	
LNC	3.869	12.646	189.25
LNC-Fe$_{0.01}$	3.881	12.682	190.99
LNC-Fe$_{0.03}$	3.878	12.710	191.14
LNC-Fe$_{0.05}$	3.885	12.682	191.45
LNC-Fe$_{0.1}$	3.879	12.708	191.19
LNC-Fe$_{0.2}$	3.893	12.671	192.05

*The average lattice parameter is calculated from the diffraction peaks of (101), (103), (110), (114) and (200) planes.

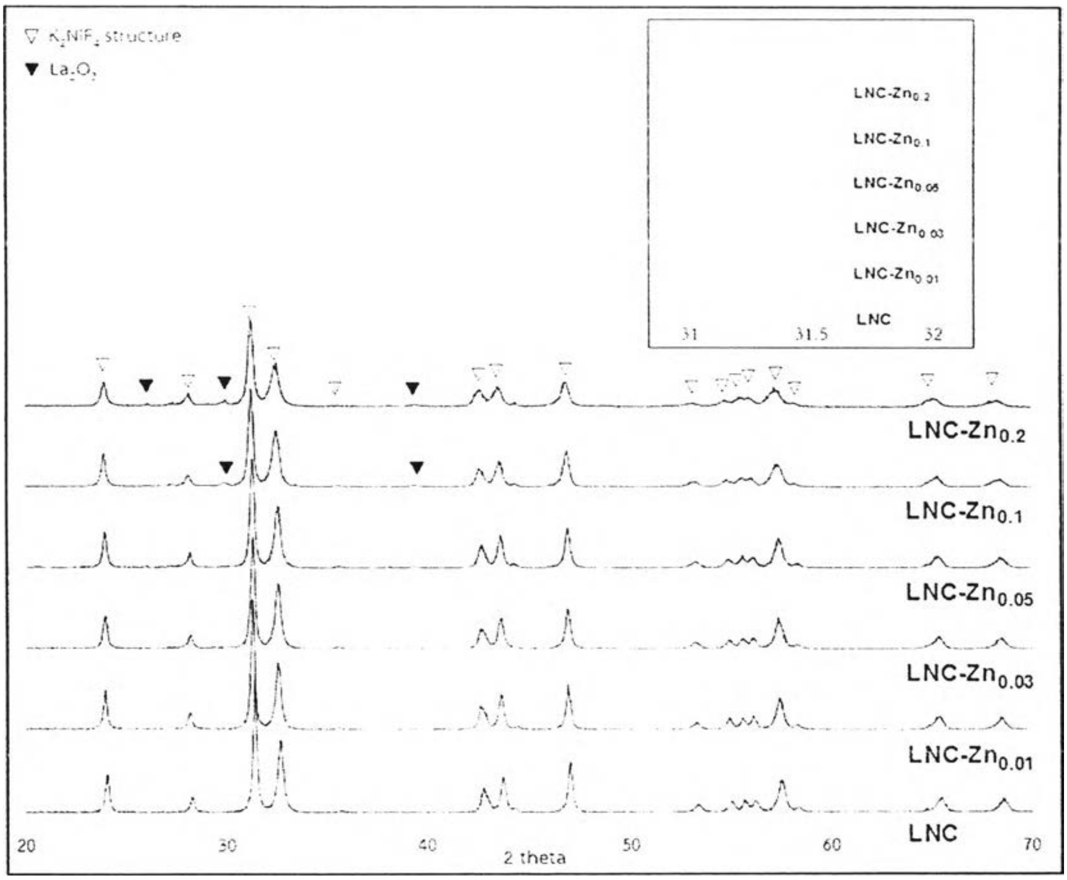

Figure 3.10 XRD patterns of LNC-Zn$_y$ discs sintered at 1350°C for 10 hours

Table 3.11 Lattice parameters and unit cell volume of LNC-Zn$_y$

Compound	* Lattice parameter		V (Å^3)
	a (Å)	c (Å)	
LNC	3.869	12.646	189.25
LNC-Zn$_{0.01}$	3.879	12.653	190.35
LNC-Zn$_{0.03}$	3.873	12.697	190.47
LNC-Zn$_{0.05}$	3.888	12.719	192.23
LNC-Zn$_{0.1}$	3.888	12.669	191.53
LNC-Zn$_{0.2}$	3.887	12.624	190.73

*The average lattice parameter is calculated from the diffraction peaks of (101), (103), (110), (114) and (200) planes.

3.4.2 SEM analyses

Figure 3.11 shows the surface microstructures of LNC-Fe$_y$ and LNC-Zn$_y$ (y=0, 0.01, 0.03, 0.05). Moreover the average grain size and calculated relative density were presented in Table 3.12. All samples reveal good densificaion and no porosity are appeared. The grain size is between 2.0 and 3.8 μm. It is known that the oxygen permeation measurement requires very dense discs (≈94% of theoretical density) and the absence of open porosity in the sample [47]. It can be seen that the density of all samples in this system is higher than 95% which is sufficient for the requirement of oxygen permeation measurement. However, there is no relationship between the density and the amount of Fe or Zn substitution.

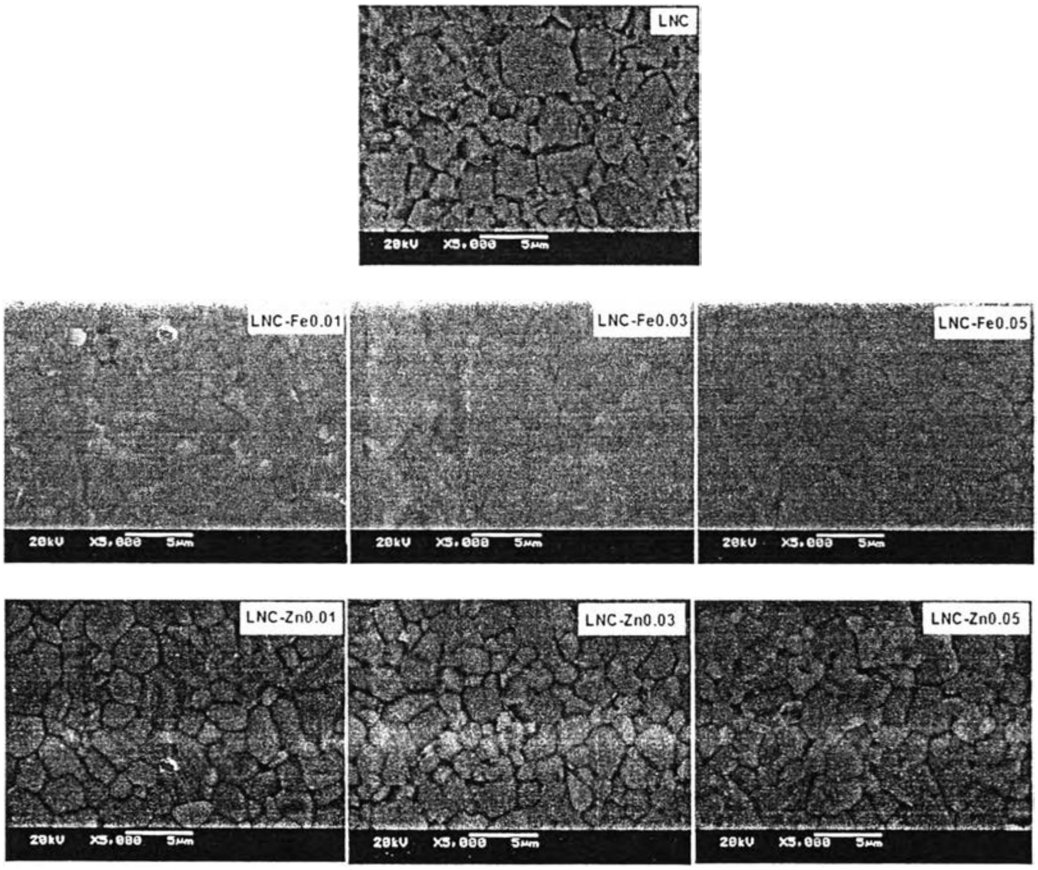

Figure 3.11 SEM images of LNC-Fe$_y$ and LNC-Zn$_y$ (y=0, 0.01, 0.03 and 0.05) discs

Table 3.12 Average grain size and relative density of LNC-Fe$_y$ and LNC-Zn$_y$ (y=0, 0.01, 0.03 and 0.05) discs

Sample	Grain size (μm)	Relative density (%)
LNC	3.8	98.94
LNC-Fe$_{0.01}$	2.9	96.83
LNC-Fe$_{0.03}$	3.6	95.98
LNC-Fe$_{0.05}$	3.8	96.53
LNC-Zn$_{0.01}$	2.6	95.79
LNC-Zn$_{0.03}$	2.1	96.98
LNC-Zn$_{0.05}$	2.0	96.44

3.4.3 Oxygen permeation analyses

The variation of oxygen permeation rate with temperature was measured on LNC-Fe$_y$ and LNC-Zn$_y$ (y=0, 0.01, 0.03 and 0.05) and the results are presented in Figure 3.12 and 3.13, respectively.

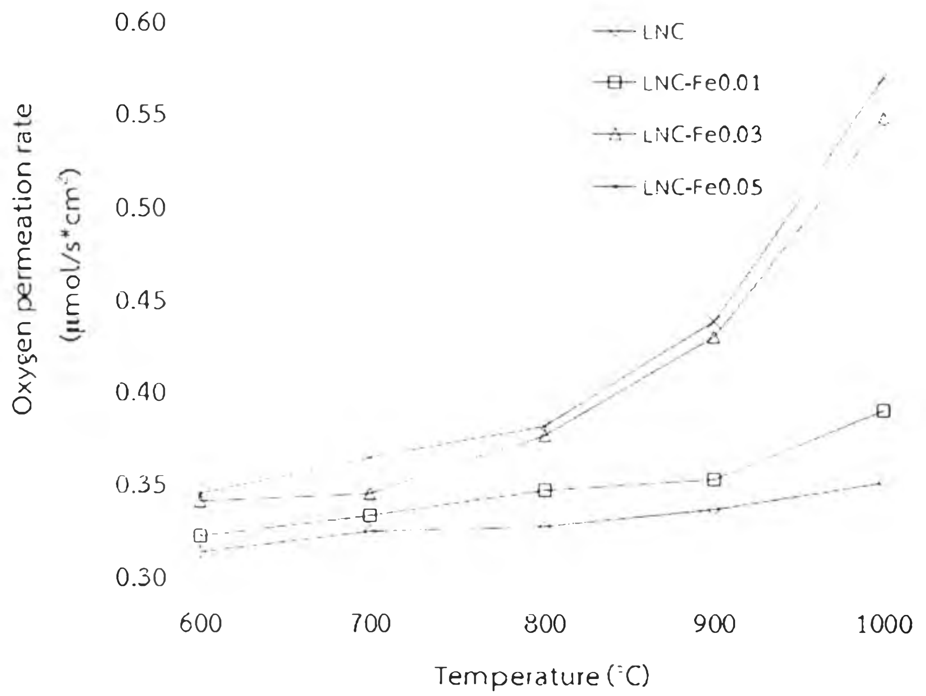

Figure 3.12 Temperature dependence of oxygen permeation for LNC-Fe$_y$ (y=0, 0.01, 0.03 and 0.05)

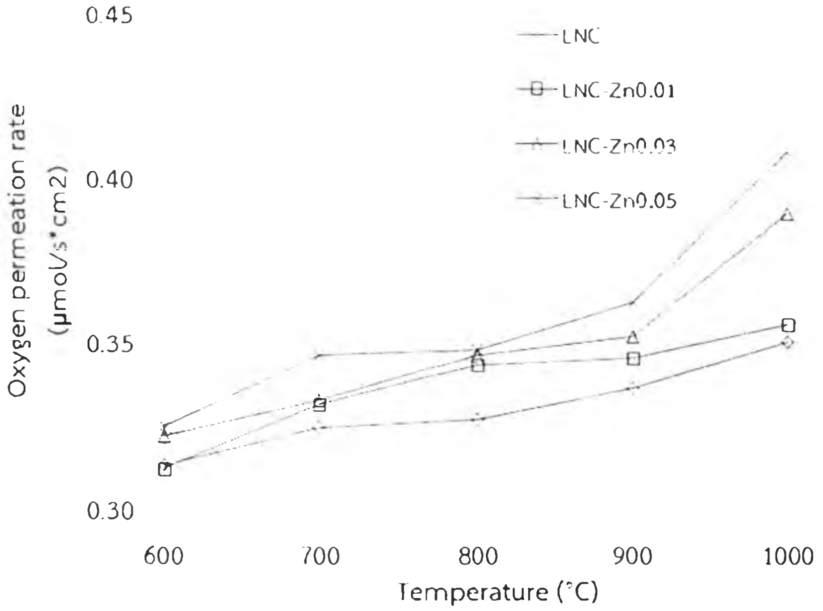

Figure 3.13 Temperature dependence of oxygen permeation for LNC-Zn_y (y=0, 0.01, 0.03 and 0.05)

It is found that the oxygen permeation rate increases with increasing temperature. At high temperature, the loss of lattice oxygen results in the increasing of concentration and mobility of oxide ion [48] and the decreasing of activation energy for the ion mobility and surface exchange [49]. Therefore the oxygen permeation rate increases with temperature. Moreover the partial substitution of B-site cations with Fe or Zn leads to the higher oxygen permeation rate. Substitution with y=0.05 shows the highest oxygen permeation rate in each series. The maximum oxygen permeation rate value is 0.57 and 0.41 μmol/s.cm^2 at 1000°C for LNC-$Fe_{0.05}$ and LNC-$Zn_{0.05}$, respectively.

The oxygen permeation rate is influenced by many structural factors such as lattice free volume of the unit cell and available channels for mobility oxide ion (saddle point) [50]. Doping B-site cation with large ionic size results in the lattice expansion which providing more space in the structure. Moreover the electrostatic force between cations and oxide ions is also weaker and the saddle point is expanded. Thus, the oxide ions easily move throughout the structure leading to the high oxygen permeation rate.

In addition, the increasing of oxygen permeation can be explained by the increased concentration of oxygen vacancies which facilitate oxide ion mobility via oxygen vacancies [34]. In case of LNC-Zn_y, Zn has a fixed valence state of +2. When doping of this ion, the preferred mechanism of charge compensation is the generation of oxygen vacancies in the structure rather than the formation of electron hole because of its unchangeable oxidation state. Miyoshi [35] reported that for $Pr_2Ni_{0.8-x}Cu_{0.2}Fe_xO_4$, the enhancement in the oxygen permeation by replacing of Ni with Fe can be explained by the increase in the amount of excess oxygen (interstitial oxygen). Since the stable valence state of Fe is +3, the concentration of Ni^{3+} decreased by substitution with Fe. Therefore the oxygen vacancies increase by the charge neutralization reaction.

The oxygen permeation in K_2NiF_4-type materials is controlled by oxide ion conductivity [51] which related to the diffusion of interstitial oxygen mainly occurring in the rock-salt layer (interstitial mechanism) and the transport of oxide ion via vacancies in the perovskite layer (vacancy mechanism) [52] as displayed in Figure 3.14. Therefore, the highest oxygen permeation rate is associated with both oxygen vacancy and interstitial oxygen.

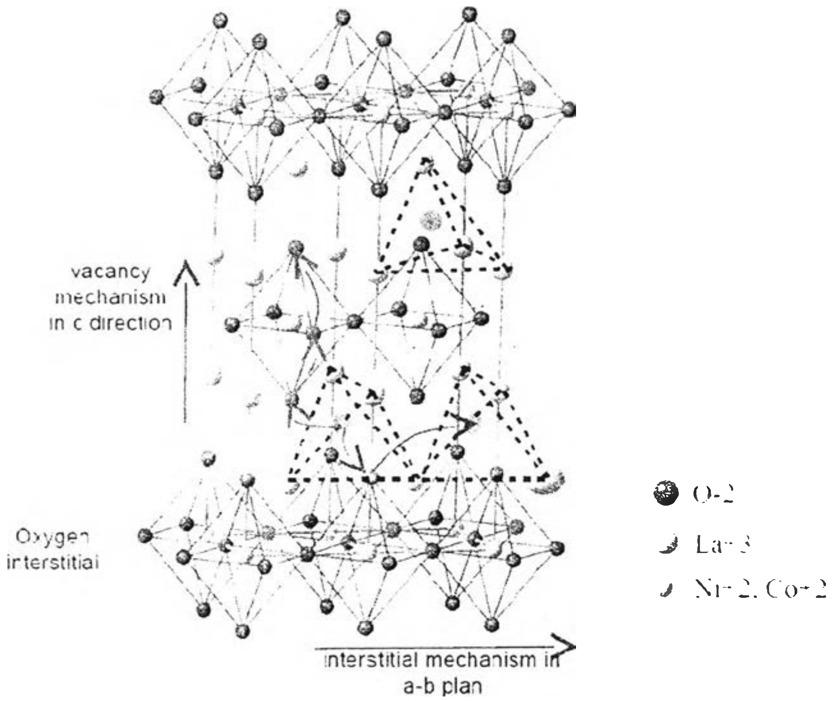

Figure 3.14 Oxygen migration path in the a-b plane and c direction

3.5 Synthesis and properties of $La_{2-x}Ca_xNi_{0.85}Co_{0.1}M_{0.05}O_4$ (M=Fe, Zn and x=0-0.7)

Based on oxygen permeation results, LNC-$Fe_{0.05}$ and LNC-$Zn_{0.05}$ provide the highest oxygen permeation rate in each series. Therefore calcium was then incorporated into both of them at La-site in order to improve the electrical conductivity.

3.5.1 XRD analyses

The XRD patterns of LNCF-Ca_x and LNCZ-Ca_x (x=0, 0.1, 0.3, 0.5 and 0.7) are presented in Figure 3.15 and 3.16, respectively. The phase is identified as K_2NiF_4-type with tetragonal structure. It is observed that all peaks shift to lower angle with increasing the calcium content compared to the undoped sample, indicating reduced lattice parameters as given in Table 3.10 and Table 3.11. This is due to the fact that substitution with smaller cation causes a reduction in lattice parameters. The samples with x=0-0.5 exhibit a pure phase without any impurity, while with higher Ca content (x=0.7), a small amount of CaO is observed. This suggests that the limitation of Ca addition is less than 0.7. Thus, LNCF-Ca_x and LNCZ-Ca_x which x=0-0.5 were selected for further study.

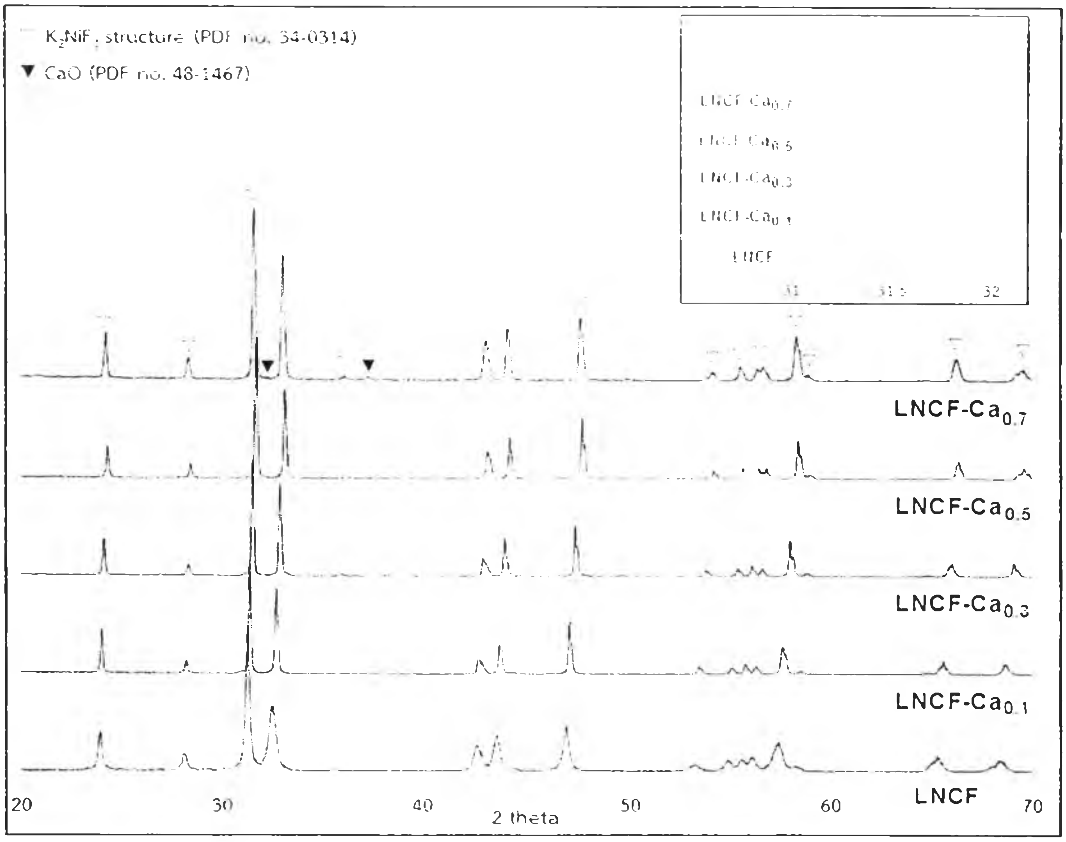

Figure 3.15 XRD patterns of LNCF-Ca_x discs sintered at 1350°C for 10 hours

Table 3.13 Lattice parameters and unit cell volume of LNCF-Ca_x

Compound	* Lattice parameter		V (Å^3)
	a (Å)	*c* (Å)	
LNCF	3.885	12.682	191.41
LNCF-$Ca_{0.1}$	3.872	12.558	188.24
LNCF-$Ca_{0.3}$	3.849	12.573	186.24
LNCF-$Ca_{0.5}$	3.819	12.570	183.32
LNCF-$Ca_{0.7}$	3.826	12.496	182.87

*The average lattice parameter is calculated from the diffraction peaks of (101), (103), (110), (114) and (200) planes.

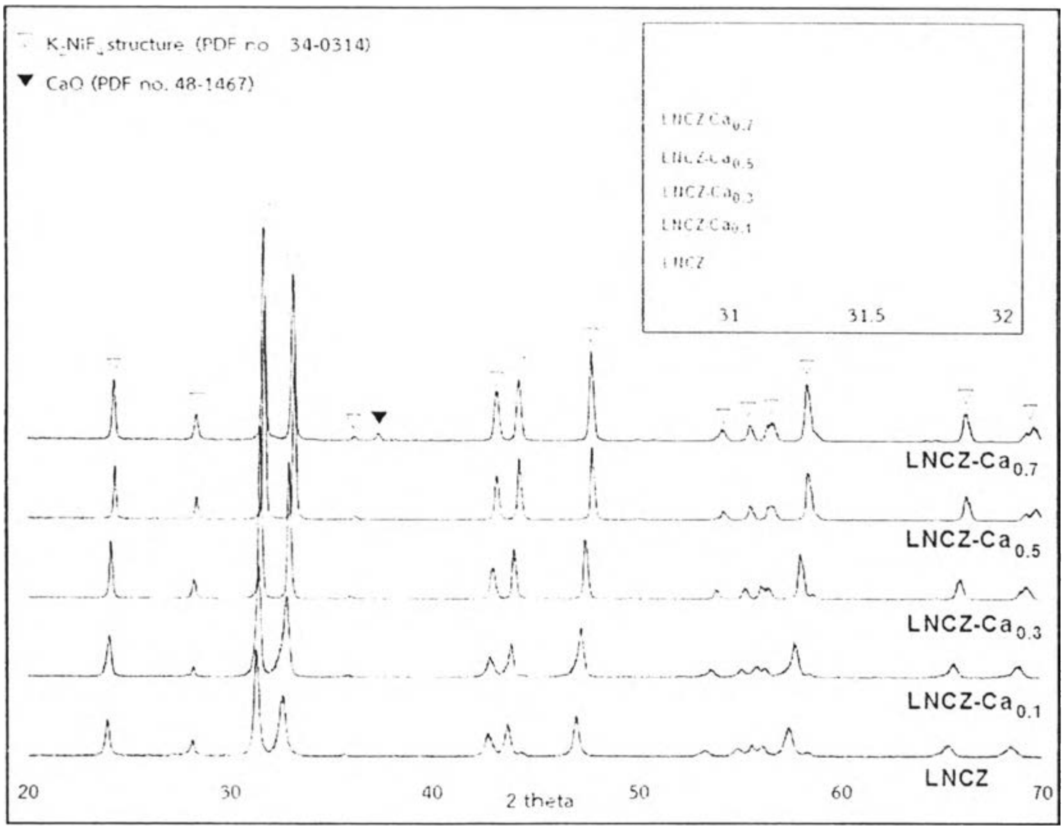

Figure 3.16 XRD patterns of LNCZ-Ca$_x$ discs sintered at 1350°C for 10 hours

Table 3.14 Lattice parameters and unit cell volume of LNCZ-Ca$_x$

Compound	* Lattice parameter		V (Å^3)
	a (Å)	*c* (Å)	
LNCZ	3.888	12.719	192.23
LNCZ-Ca$_{0.1}$	3.871	12.649	189.57
LNCZ-Ca$_{0.3}$	3.846	12.593	186.28
LNCZ-Ca$_{0.5}$	3.817	12.510	182.25
LNCZ-Ca$_{0.7}$	3.823	12.497	182.67

*The average lattice parameter is calculated from the diffraction peaks of (101), (103), (110), (114) and (200) planes.

3.5.2 SEM analyses

Figure 3.17 presents the SEM images of LNCF-Ca_x and LNCZ-Ca_x (x=0, 0.1, 0.3 and 0.5). The microstructure of all samples indicates densified membranes. With increasing Ca content, the large grain size is obtained which is consistent with the result of relative density calculation in Table 3.15. The average grain size varies from 2.0 to 6.9 µm and the calculated density is over 95 %. It can be seen that the grain size of the Ca-doped sample is higher than that of the undoped one, suggesting that the calcium dopant facilitates LNCF and LNCZ to form the dense microstructure.

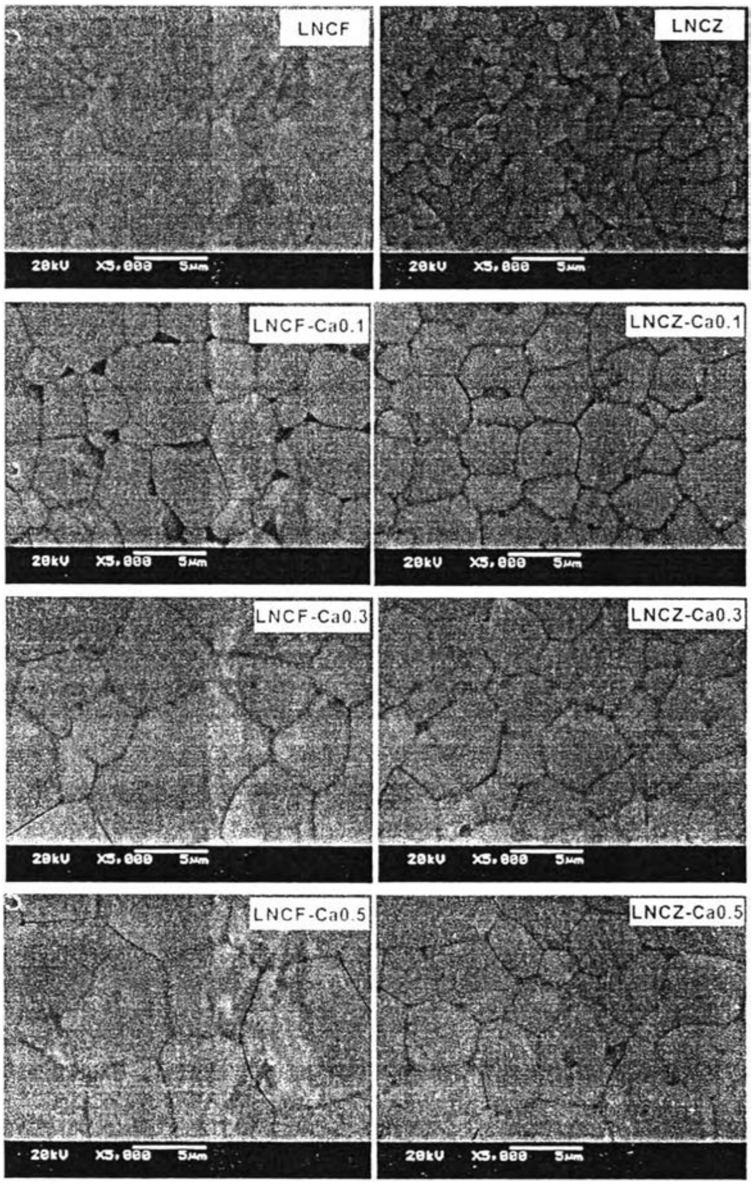

Figure 3.17 SEM images of LNCF-Ca_x and LNCZ-Ca_x (x=0, 0.1, 0.3 and 0.5) discs

Table 3.15 Average grain size and relative density of LNCF-Ca_x and LNCZ-Ca_x (x=0, 0.1, 0.3 and 0.5) discs

Sample	Grain size (μm)	Relative density (%)
LNCF	3.8	96.53
LNCF-$Ca_{0.1}$	4.8	97.21
LNCF-$Ca_{0.3}$	6.2	98.45
LNCF-$Ca_{0.5}$	6.9	98.46
LNCZ	2.0	96.44
LNCZ-$Ca_{0.1}$	4.0	96.78
LNCZ-$Ca_{0.3}$	4.2	97.45
LNCZ-$Ca_{0.5}$	5.1	97.69

3.5.3 Electrical conductivity analyses

Figure 3.18 and 3.19 displays the temperature dependence of the electrical conductivity of LNCF-Ca_x and LNCZ-Ca_x (x=0, 0.1, 0.3, 0.5 and 0.7) and the data are summarized in table 3.16 and 3.17, respectively.

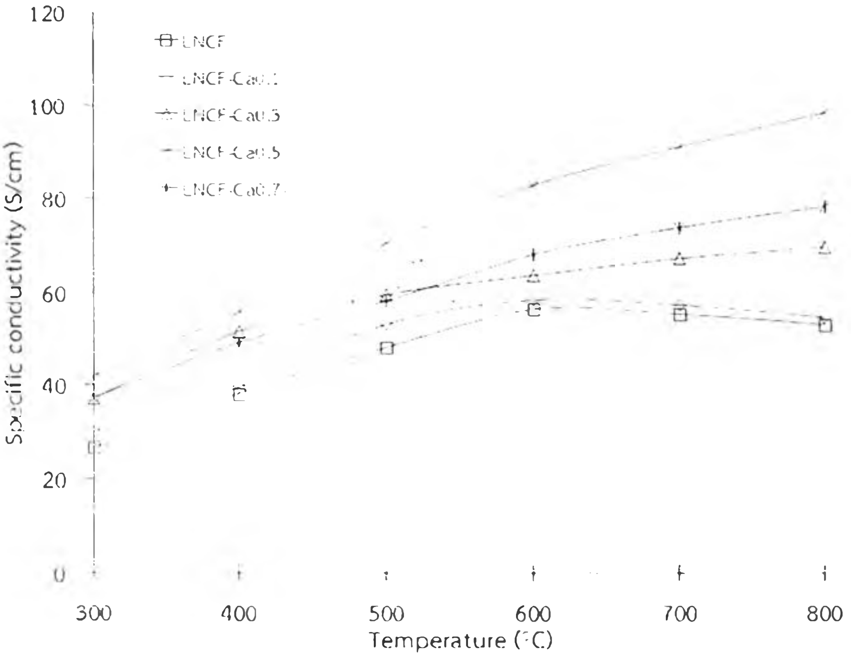

Figure 3.18 Temperature dependence of the specific conductivity (σ) of LNCF-Ca_x (x=0-0.7)

Table 3.16 The specific conductivity of LNCF-Ca$_x$ (x=0-0.7)

Sample	Specific conductivity (S/cm)						
	300°C	400°C	500°C	600°C	700°C	800°C	σ_{max} (T, °C)
LNCF	26.7	38.2	48.4	56.5	55.5	53.3	56.5 (600)
LNCF-Ca$_{0.1}$	30.1	39.7	53.3	58.5	57.4	54.8	58.5 (600)
LNCF-Ca$_{0.3}$	37.2	51.8	59.7	63.9	67.5	69.9	69.9 (800)
LNCF-Ca$_{0.5}$	41.9	55.9	70.6	82.9	91.1	98.4	98.4 (800)
LNCF-Ca$_{0.7}$	37.3	49.3	58.3	68.2	73.9	78.5	78.5 (800)

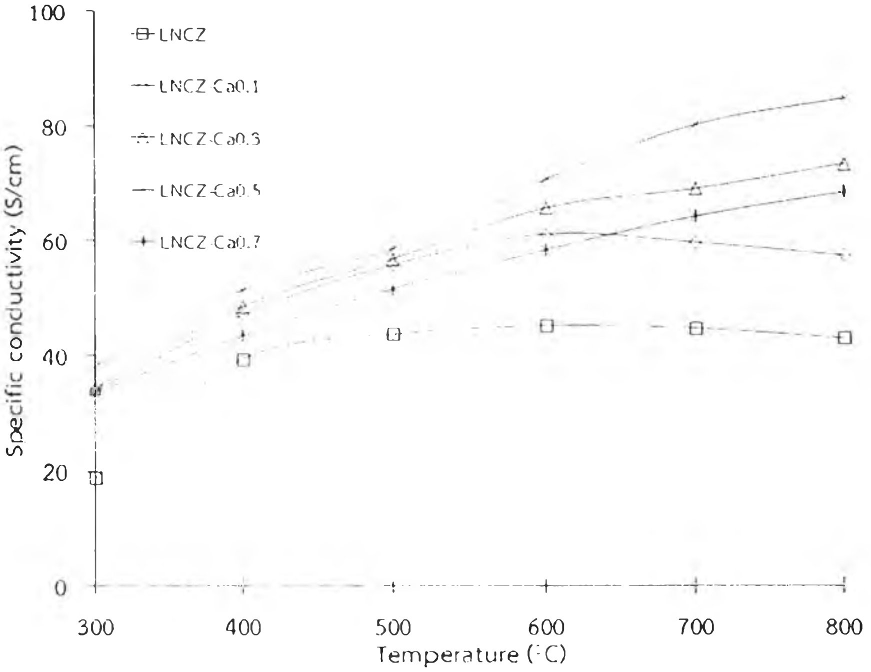

Figure 3.19 Temperature dependence of the specific conductivity (σ) of LNCZ-Ca$_x$ (x=0-0.7)

Table 3.17 The specific conductivity of LNCZ-Ca$_x$ (x=0-0.7)

Sample	Specific conductivity (S/cm)						
	300°C	400°C	500°C	600°C	700°C	800°C	σ_{max} (T, °C)
LNCZ	19.0	39.4	43.7	45.2	44.8	43.0	45.2 (600)
LNCZ-Ca$_{0.1}$	33.8	47.1	55.9	61.2	59.8	57.4	61.2 (600)
LNCZ-Ca$_{0.3}$	34.4	48.6	56.9	65.8	69.1	73.4	73.4 (800)
LNCZ-Ca$_{0.5}$	38.1	51.5	58.7	70.7	80.2	84.9	84.9 (800)
LNCZ-Ca$_{0.7}$	33.6	43.5	51.7	58.4	64.3	68.5	68.5 (800)

Both LNCF-Ca_x and LNCZ-Ca_x have the similar trend of electrical conductivity. For x>0.1 the conductivity increases with temperature which indicates a semiconducting behavior in whole temperature range while for x=0 and 0.1 the conductivity increases to the temperature of 600°C and remains constant afterwards. This suggests the semiconducting behavior only at low temperature. The conductivity do not increase at high temperature because of the reduction of B^{4+} to B^{3+} resulting in the creation of oxygen vacancies and the decreased covalency of B-O bonds [53].

In addition with increasing calcium substitution, the conductivity increases and achieves a maximum value at x=0.5, and becomes decreasing with more calcium content (x=0.7). The increased conductivity can be explained by the increase in B^{4+} cations caused by substitution of trivalent cation (La^{3+}) with bivalent cation (Ca^{2+}). On the other hand, the decreased conductivity when x=0.7 may be due to the strain caused by high calcium content substituted into the lattice and the existence of impurity phase, CaO, which introduces scattering effect of the charge carrier [54]. It is observed that the maximum conductivity is 98.4 for S/cm for LNCF-$Ca_{0.5}$ and 84.9 for LNCZ-$Ca_{0.5}$ at 800°C. Therefore LNCF-$Ca_{0.5}$ and LNCZ-$Ca_{0.5}$ were selected to study the electrochemical properties in the next experiment.

3.6 Electrochemical analyses

LSN-$Ca_{0.2}$, LSNC-$Ca_{0.2}$, LNCF-$Ca_{0.5}$ and LNCZ-$Ca_{0.5}$ which had the highest electrical conductivity in each series were chosen to investigate the electrochemical properties. However before the electrochemical test, it is necessary to check the possible chemical reaction of cathode materials and electrolyte (LSGM) because the phase reaction occurring at the interface may create an insulating interfacial layer. This layer can block oxygen transfer between the cathode and electrolyte resulting in a decrease in cell performance [55].

3.6.1 Material compatibility

In order to check the compatibility between the cathode and the LSGM electrolyte, cathode materials and LSGM in 1:1 weight ratio were mixed together and then fired at 1000°C for 10 hours in air and determined the phase appeared by XRD technique.

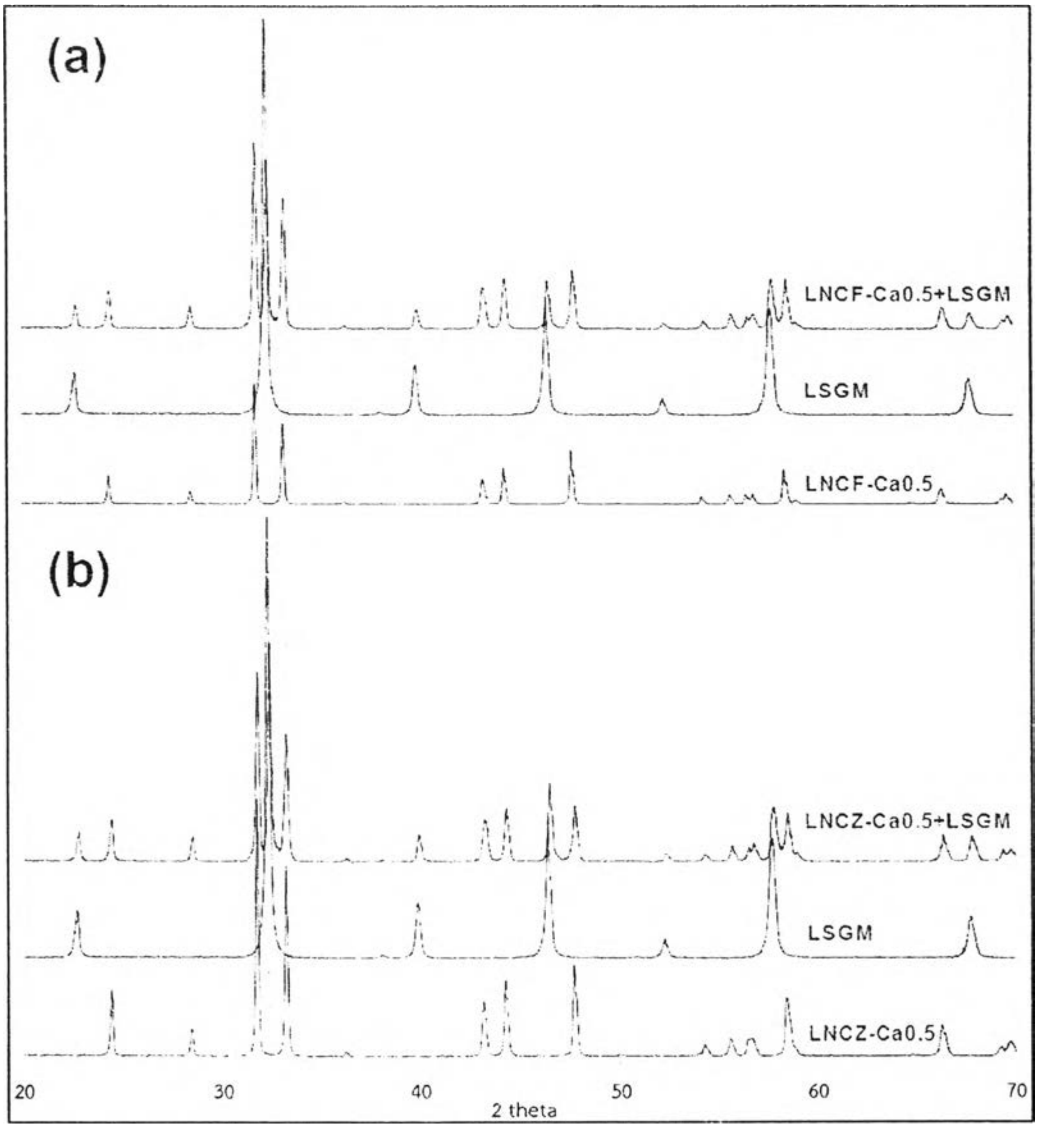

Figure 3.20 XRD patterns of LNCF-$Ca_{0.5}$ -LSGM (a) and LNCZ-$Ca_{0.5}$ -LSGM (b) mixtures after fired at 1000°C for 10 hours

For comparison, the XRD pattern of each cathode, LSGM and mixed cathode-LSGM are shown in Figure 3.20. It can be seen that the structure of the mixture is not changed and no new diffraction peaks are observed in LNCF-$Ca_{0.5}$ and LNCZ-$Ca_{0.5}$ suggesting that there are no serious reaction occurred between them. Therefore it is reasonable to conclude that LNCF-$Ca_{0.5}$ and LNCZ-$Ca_{0.5}$ are stable and do not react with LSGM electrolyte at 1000°C.

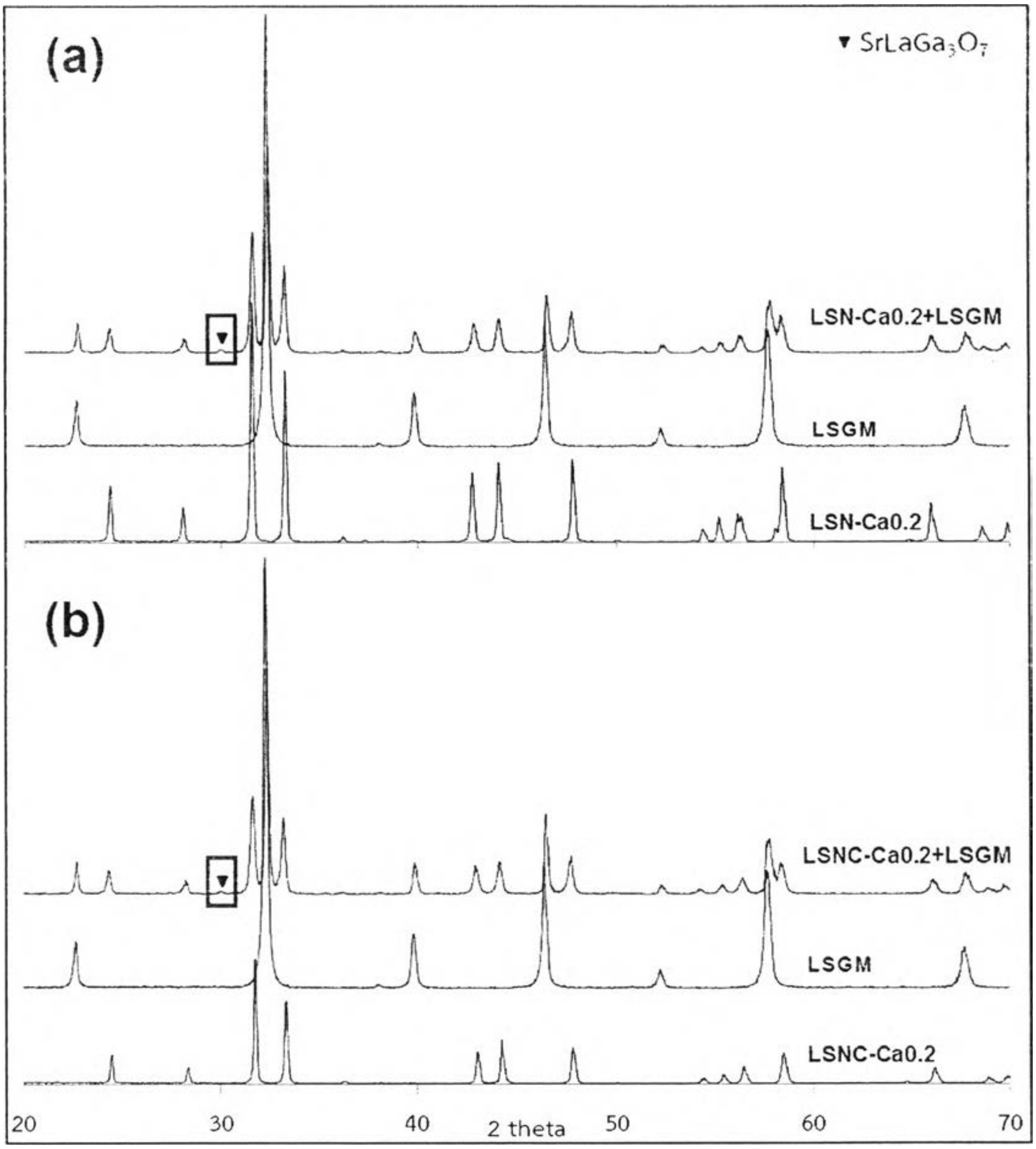

Figure 3.21 XRD patterns of LSN-Ca$_{0.2}$ -LSGM (a) and LSNC-Ca$_{0.2}$ -LSGM (b) mixtures after fired at 1000°C for 10 hours

In case of LSN-Ca$_{0.2}$ and LSNC-Ca$_{0.2}$, a new small peak is observed at 2θ of 30 degree corresponding to SrLaGa$_3$O$_7$ (JCPDS 45-0637), indicating that they react with LSGM electrolyte to form a new phase at 1000°C. The reactivity of these materials leads to the negative effect on the cell performance. Therefore in order to avoid this unwanted phase, the compatibility at 950°C and 900°C was then studied.

XRD patterns of mixed powder of LSN-Ca$_{0.2}$ and LSNC-Ca$_{0.2}$ with LSGM electrolyte at 950°C and 900°C are presented in Figure 3.22-3.23. There is a new peak appeared at 2θ of 30 degree corresponding to $SrLaGa_3O_7$. It can be concluded that at 950°C and 900°C LSN-Ca$_{0.2}$ and LSNC Ca$_{0.2}$ are unstable and react with LSGM electrolyte to form a resistance phase.

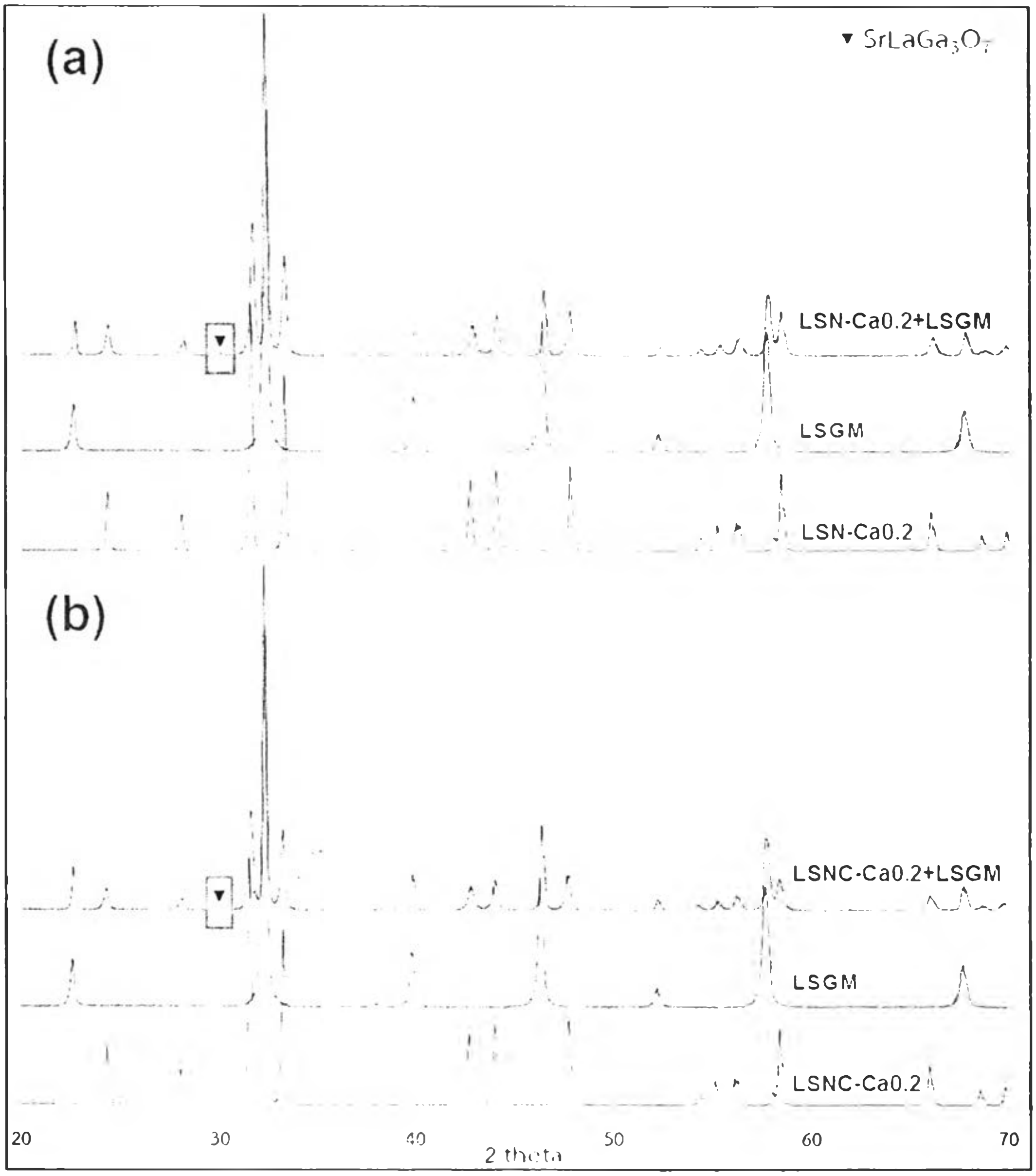

Figure 3.22 XRD patterns of LSN Ca$_{0.2}$ -LSGM (a) and LSNC Ca$_{0.2}$ LSGM (b) mixtures after fired at 950°C for 10 hours

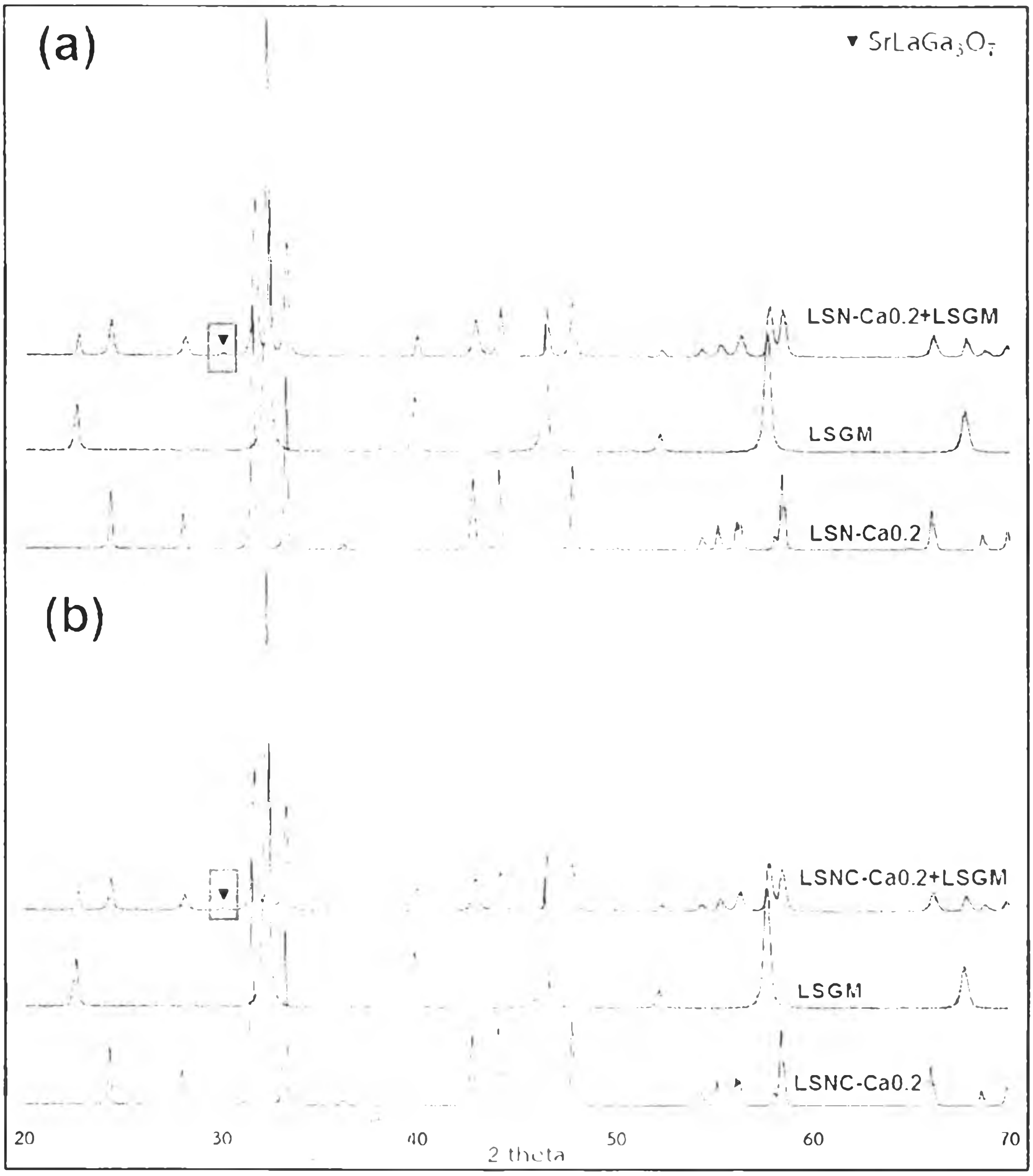

Figure 3.23 XRD patterns of LSN-Ca$_{0.2}$-LSGM (a) and LSNC-Ca$_{0.2}$-LSGM (b) mixtures after fired at 900°C for 10 hours

3.6.2 Impedance and single cell performance analyses

LNCF-Ca$_{0.5}$ and LNCZ-Ca$_{0.5}$ were chosen to study the electrochemical property with LSGM supported single cell because they did not react with LSGM electrolyte at operating temperature. The polarization resistance and single cell performance in SOFC were measured at 800°C and 700°C. The impedance spectra, current-voltage and corresponding power density curves are displayed in Figure 3.24-3.25.

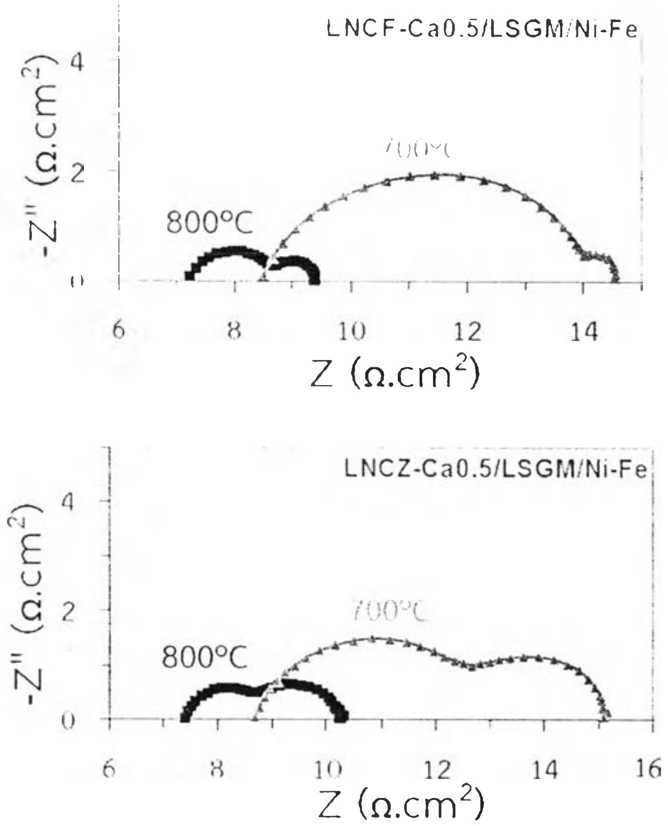

Figure 3.24 The AC impedance spectra of LNCF-Ca$_{0.5}$/LSGM/Ni-Fe and LNCZ-Ca$_{0.5}$/LSGM/Ni-Fe

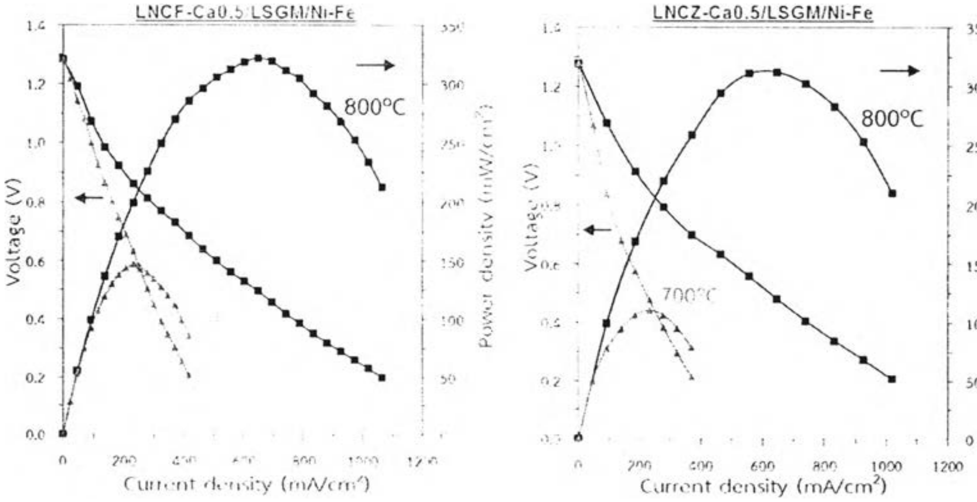

Figure 3.25 I-V curves and corresponding power density curves of LNCF-Ca$_{0.5}$/LSGM/Ni-Fe and LNCZ-Ca$_{0.5}$/LSGM/Ni-Fe

From Nyquist plot, it is found that all samples contain two separate arcs in each spectrum. This means that there are at least two electrode processes corresponding to the oxygen reduction reactions over the cell. The first arc at high frequency region is related to charge transfer reaction at electrode/electrolyte interface. While the other arc at low frequency region is related to the diffusion processes namely the oxygen adsorption/desorption on the cathode surface and the diffusion of oxygen ion [56]. The ohmic resistance (R_o) including the electrolyte, electrodes, current collectors and lead wires, is obtained from the intercept value at high frequency region with the real axis. The width between the high and the low frequency intercept is the polarization resistance (R_p) and the sum of R_o and R_p gives the total resistance of the cell [57-59]. For IT-SOFC, the cathode requires low polarization. It is observed that the obtained polarization resistance is in agreement with the data obtained from the cell performance test. The summarized total polarization resistances and power densities of each sample are listed in Table 3.18.

Table 3.18 Polarization resistance and power density of LNCF-$Ca_{0.5}$/LSGM/Ni-Fe and LNCZ-$Ca_{0.5}$/LSGM/Ni-Fe

Single cell	800°C		700°C	
	R_p (Ω.cm^2)	P (mW/cm^2)	R_p (Ω.cm^2)	P (mW/cm^2)
LNCF-$Ca_{0.5}$/LSGM/Ni-Fe	2.1	322	6.0	147
LNCZ-$Ca_{0.5}$/LSGM/Ni-Fe	2.9	312	6.4	111

It can be seen that the polarization resistance decreases with increasing operating temperature. Since at high temperature several processes such as migration of charge, gas transport and electrochemical reaction at TPB sites are enhanced resulting in the reduction of polarization resistance.

The maximum power density of the single cell with LNCF-$Ca_{0.5}$ is slightly higher than LNCZ-$Ca_{0.5}$. This is possibly due to the fact that LNCF-$Ca_{0.5}$ has the higher oxygen mobility compared to LNCZ-$Ca_{0.5}$, as seen in oxygen permeation results. With high oxygen diffusion properties, the oxygen rapidly transports through the material resulting in the enhancement of electrocatalytic properties. The maximum power densities of LNCF-$Ca_{0.5}$ and LNCZ-$Ca_{0.5}$ are 322 and 312 mW/cm^2, respectively. These value are higher than that of 226 mW/cm^2 at 800°C for La_2NiO_4 electrode on LSGM electrolyte reported by Escudero [29], suggesting that good performance can be obtained for the single cell using LNCF-$Ca_{0.5}$ and LNCZ-$Ca_{0.5}$ as cathode and LSGM as electrolyte.